

RESEARCH ARTICLE

10.1029/2018JB016430

Key Points:

- An improved direct simulation method is presented to investigate the spontaneous imbibition behavior in complex shale porous structures
- Pore size and wettability heterogeneity lead to nonuniform propagation and distribution of fracturing fluid
- Reopening of larger pores during spontaneous imbibition process cause a great recovery of the apparent gas permeability

Correspondence to:

Y. Ju and M. Wang,
juy@cumtb.edu.cn;
mrwang@tsinghua.edu.cn

Citation:

Zheng, J., Ju, Y., & Wang, M. (2018). Pore-scale modeling of spontaneous imbibition behavior in a complex shale porous structure by pseudopotential lattice Boltzmann method. *Journal of Geophysical Research: Solid Earth*, 123, 9586–9600. <https://doi.org/10.1029/2018JB016430>



Received 21 JUL 2018

Accepted 5 NOV 2018

Accepted article online 12 NOV 2018

Published online 24 NOV 2018

Pore-Scale Modeling of Spontaneous Imbibition Behavior in a Complex Shale Porous Structure by Pseudopotential Lattice Boltzmann Method

Jiangtao Zheng^{1,2}, Yang Ju^{1,3} , and Moran Wang² ¹State Key Laboratory of Coal Resources and Safe Mining, China University of Mining and Technology, Beijing, China,²Department of Engineering Mechanics, Tsinghua University, Beijing, China, ³State Key Laboratory for Geomechanics and Deep Underground Engineering, China University of Mining and Technology, Xuzhou, China

Abstract Spontaneous imbibition of fracturing fluid into shale matrix is one of the primary reasons for the low flowback rate in shale gas wells after the hydraulic fracturing. This leads to concerns of impacts on both environment and shale gas production. A direct pore-scale simulation is crucial to gain a deep understanding of spontaneous imbibition behavior and its impacts. The porous structures in the shale matrix are characterized by not only a geometrical complexity but also a mixed wettability, which bring great challenges to simulation methods. An improved pseudo-potential lattice Boltzmann method is proposed to simulate the spontaneous imbibition behavior in a reproduced three-dimensional porous structure of shale. The results show that the nanoscale hydrophilic pores provide the driving force and a storage place for the residual treatment fluid. The pore size and wettability heterogeneity lead to the nonuniform menisci propagation and fracturing fluid distribution in the model. Specifically, the fracturing fluid imbibed quicker in the larger pores at the early stage and gradually migrated into the smaller pores during the process. With a limited volume of the fracturing fluid, a portion of the larger pores was finally reopened. The analysis of saturation and apparent gas permeability data during the spontaneous imbibition process showed a great recovery of the model permeability along with the reopened pores. These results provide direct evidence of the residual fracturing fluid migration pattern in the shale reservoir and its influence on shale gas production.

Plain Language Summary Hydraulic fracturing is widely employed to stimulate a shale gas reservoir for a better production. After fracturing, a substantial amount of the fracturing fluid stays in the reservoir even after a period of flowback operations. It is believed that the residual treatment fluid is imbibed into the surrounding shale matrix. However, whether these trapped fracturing fluids impact the shallow aquifers and the shale gas production rates remains to be fully understood. A pore-scale simulation is performed in this work to directly investigate the migration of the fracturing fluid in a reproduced porous structure of shale. The results showed that (1) the nanoscale pores in the shale matrix provide the driving force, namely, the capillary force, and the storage space for holding the fracturing fluids. (2) The nonuniform spontaneous imbibition in the complex shale porous structure results in the fracturing fluid-filled small pores and a portion of reopened large pores. The reopening of the large pores leads to a great recovery of the model transport property of the shale gas. These results can be served as evidence for answering the engineering related problems, such as the low flowback rate of the fracturing fluid and the relatively high gas production after the shut-in operation.

1. Introduction

Hydraulic fracturing has been widely used for economically recovering the natural gas in extremely low permeability shale layers. During the process, a large amount of water-based fracturing fluids (typically approximately 20,000 m³ per well) is injected to stimulate the reservoir in order to create extra transport channels for the trapped gas to flow out. Once completed, the fluids are allowed to flowback up to the ground for several days. However, usually less than half of them can be recovered (Roychaudhuri et al., 2013; Singh, 2016). This has raised two main concerns: (1) where does the water migrate (Engelder et al., 2014; O'Malley et al., 2016) and will it contaminate the shallow drinking water (Birdsell et al., 2015)? (2) How does the remaining fracturing fluid in the reservoir impacts the shale gas production rates (Bertoncello et al., 2014; Yan et al., 2015)?

The first question causes great environmental and geological concerns, as the migration of the fracturing fluids may contaminate the underground water and trigger nearby faults to slip. Even now, there are still great debates about whether the detrimental fracturing fluid migrates beyond the shale layer through the natural permeable ways and causes further environmental issues (Engelder, 2012; Warner et al., 2012). Warner et al. (2012) argued that the fracturing fluid possibly migrates upward through the natural connectivity between the shale reservoir and the shallow water aquifers. However, as claimed by Engelder et al. (2014), the shale reservoir should be tight enough to sequester the over pressured gas on a geological time scale. Moreover, the water saturation in the deep underground shale layers is usually much smaller than the irreducible water saturation, which provides a great potential to host the fracturing fluid. It was inferred that the main mechanisms responsible for the fracturing fluids spontaneously penetrated into the formation include capillary forces (Xu & Dehghanpour, 2014), osmotic forces (Zhou et al., 2016), absorption, and clay hydration (Dehghanpour et al., 2012; Singh, 2016). Since the nanoscale pores dominated in the shale, the induced high capillary force was considered to be the primary factor for the fracturing fluid spontaneously imbibing into the formation (Yang et al., 2017).

For the second one, a great debate also appeared about whether the low flowback rate is good or bad for the shale gas production. The previous work on tight gas sandstone has demonstrated that the low flowback rate would significantly reduce the gas production rate due to the decrease of the relative gas permeability in the presence of water (Shanley et al., 2004; Shaoul et al., 2011). In agreement with this concept, the low flowback rate was assumed to decrease the production of the shale gas. For example, Chakraborty et al. (2017) showed a reduction of 90–99% of the shale core permeability due to the water imbibition and argued that this could be detrimental to the long-term shale gas production. However, *in situ* observations (Ghanbari & Dehghanpour, 2016; Wang et al., 2012) have shown that a shale gas well with a very low flowback rate could also have an economic production. Moreover, a shut-in period before the gas production is designed in many recent shale gas well exploitations for a higher initial production rate (Bertoncello et al., 2014). This shut-in period further facilitates the imbibition of fracturing fluid into the formation, which results in an even lower flowback rate. Several studies have been conducted to provide a plausible explanation for the low flowback rate and the high initial gas production. For instance, Abbasi et al. (2014) investigated the flowback behavior of several low permeability gas and oil wells and pointed out that the gas breakthrough is much quicker in a shale gas well than that in a tight sandstone gas wells. Liu, Lai, et al. (2016), Liu, Ranjith, et al. (2016), and Roshan et al. (2015) postulated that the lamination feature of shale and imbibition induced microfractures facilitate the shale gas production. Furthermore, based on the simulation results, Ghanbari et al. (2013) argued that a low flowback rate is an indication of more contact areas of the fluid with the shale matrix, or in other words, an indication of a good fracturing degree. Several studies (Cheng, 2012; Dehghanpour et al., 2013; Fakcharoenphol et al., 2013) argued that the fracturing fluid in the fractures transferred into the shale matrix during the shut-in period and thus allowed for the shale gas to flow at higher rates from the fractures.

A detailed investigation of the spontaneous imbibition behavior of the fracturing fluid in the shale matrix and its control mechanisms are crucial for answering the above questions. Several theoretical and experimental works have been performed to gain a deeper understanding of the spontaneous imbibition in a shale reservoir and its influence on the gas production. The classical Lucas-Washburn (LW) equation (Lucas, 1918; Washburn, 1921) states that the spontaneous imbibition length is proportional to \sqrt{t} . This relationship has been safely extended to the homogeneous porous structures (Gruener & Huber, 2011). However, whether the relationship still applies for shale, whose porous structure shows not only geometrical complexity but also a mixed wettability, needs further investigation. Roychaudhuri et al. (2013) observed a transition imbibition behavior from the square root of time to a lower rate and argued that this was caused by the multiporosity nature of the shale samples. Cai and Yu (2011) considered the porous structure in rock as a bundle of tortuous capillaries and claimed that the fractal characteristic of these capillaries was responsible for the deviation from the LW equation. Hu et al. (2015) claimed that the low pore connectivity in shale is responsible for the significant deviation of the imbibition time exponent from 0.5. In contrast, Liu, Lai, et al. (2016) and Liu, Ranjith, et al. (2016) claimed that the strong solid-liquid interaction in the shale actually led to the lower imbibition time exponent. Several other mechanisms, such as the water absorption, clay hydration, osmotic effects, and induced microfractures during the imbibition, were blamed for the deviation of the classical imbibition time exponent (Dehghanpour et al., 2013; Roshan et al., 2015; Zhou et al., 2016). However, by only

focusing on the capillary force induced imbibition, certain difficulties exist in the analysis. For example, Ghanbari and Dehghanpour (2015) argued that the macroscopic contact angle obtained by traditional test method cannot fully explain the wettability property of a shale due to its heterogeneous mineral composition and pore connectivity. Xu and Dehghanpour (2014) inferred that the water wet pores have a higher connectivity than the oil wet organic pores. The spontaneous imbibition behavior in the shale cannot be fully understood without the detailed pore connectivity and wettability information (Gao & Hu, 2016b; Lan et al., 2015; Xu & Dehghanpour, 2014; Yang et al., 2017). As discussed, direct investigations with a focus on the pore scale phenomena would be important for a variety of fundamental purposes.

The recently developed imaging method and image-based fluid transport modeling in the microscale and mesoscale become valuable and necessary tools to understand the effective macroscopic rock properties, especially for those highly influenced by the pore geometry and wettability. The fast development of imaging methods, such as the nanoscale computer tomography (nano-CT) and the focused ion beam scanning electron microscope, greatly facilitate the observation of the three-dimensional nanoscale porous structure in shale (Arshadi et al., 2017; Desbois et al., 2011; Ju, Gong, et al., 2017; Kelly et al., 2016; Wildenschild & Sheppard, 2013; Ye et al., 2017; Zolfaghari et al., 2017). For example, Chalmers et al. (2012) investigated the pore size distribution and pore geometry of several main shale reservoirs in the United States by porosimetry and SEM imaging. Based on the SEM images, Loucks et al. (2012) classified the pores in the shale into interparticle pores, intraparticle pores, organic-matter pores, and fractures, which all have a different connectivity. The nano-CT was employed to investigate the pore distribution and related imbibition process in a nondestructive way (Akbarabadi & Piri, 2014; Chakraborty et al., 2017). Andrew et al. (2014) investigated the contact angle at the pore scale through micro-CT imaging. Moreover, several attempts were carried out to investigate the multiscale pores in shale by integrating different methods (Clarkson et al., 2016; Curtis et al., 2010; Houben et al., 2013; Nia et al., 2016). Compared with the success in obtaining the pore morphology, the direct investigation of the dynamic fluid flow behavior by experimental methods, such as the spontaneous imbibition in these porous structures, encountered great challenges, especially for shales.

Alternatively, numerical methods provide an economical and effective way to unveil the flow dynamics in the complex porous structures in shale. Two distinct modeling methods, namely, direct modeling (Chen & Gary, 1998) and pore network modeling (Piri & Blunt, 2005; Zolfaghari & Piri, 2017a, 2017b), are widely used to study the multiphase flow in porous media (Blunt et al., 2013). This work aims at directly investigating the spontaneous imbibition behavior in the complex porous structure in a shale through a simulation method. Among various kinds of direct simulation methods, the lattice Boltzmann method (LBM) shows its versatility in modeling problems that involve complicated boundary conditions and multiphase interfaces (Aidun & Clausen, 2010; Chen & Gary, 1998). There are four basic LBMs, namely, the color-fluid model, the pseudo-potential model (or SC-LBM), the free-energy model, and the mean-field theory model (Aidun & Clausen, 2010). Among these methods, the SC-LBM has been widely applied to investigate the multiphase flows due to its conceptual simplicity and computational efficiency (Li et al., 2016). It represents the interaction forces between the different fluid phases by using a local density dependent pseudopotential (Shan & Chen, 1993, 1994). The separation of the two phases happens automatically and introduces a surface tension automatically when the interaction forces are strong, that is, the negative strength factor is below a critical value in the system. In addition, the different contact angles can be implemented by properly including the adhesive force between the fluid nodes and solid nodes. The accurate introduction of the surface tension and contact angle in the model permits the simulation of capillary phenomena, such as spontaneous imbibition. While simulating the spontaneous imbibition by SC-LBM achieved great success in simple geometries, such as regularly shaped tubes and channels (Raikimäki et al., 2002; Son et al., 2016), the simulation involved complex geometries and mixed wettability results in practical difficulties, such as the unphysical fluid density accumulation near the hydrophilic corner and a stability issue related to the mixed wettability (De Maio et al., 2011; Zheng et al., 2018). The imbibition in the complex geometries involves intricate interface propagations such as the interface break-up and coalescence. The mixed wettability further complicates the imbibition process. These facts bring forth significant numerical challenges.

In this work, an improved SC-LBM is presented to simulate the complex spontaneous imbibition behavior in a reproduced three-dimensional porous structure of a shale. The migration of the fracturing fluid and its impact on the shale permeability are analyzed. The organization of the paper is as follows. In section 2, the basic algorithm and improvement of the SC-LBM are presented. Section 3 shows the simulation results of the

spontaneous imbibition in a reproduced three-dimensional shale porous structure. Some useful discussions are presented in section 4. We make concluding remarks in section 5.

2. Materials and Methods

2.1. Model Description

An improved single-component two-phase SC-LBM in three dimensions was employed in this work. The improved model modified the interaction force between the fluid nodes and solid nodes and has a better control of the fluid density accumulation near the solid nodes. The model inherited the advantages of the original SC-LBM, such as an automatic phase separation, a relatively high-density ratio between the two phases, conceptual simplicity, and computational efficiency.

The LBM is a mesoscopic method, which describes the fluid motion by a set of particle distribution functions. The evolution of these particle distribution functions with the single relaxation collision operator is given by

$$f_{\alpha}(\mathbf{x} + \mathbf{e}_{\alpha}\Delta t, t + \Delta t) - f_{\alpha}(\mathbf{x}, t) = \frac{\Delta t}{\tau} [f_{\alpha}(\mathbf{x}, t) - f_{\alpha}^{\text{eq}}(\mathbf{x}, t)], \quad (1)$$

where $f_{\alpha}(\mathbf{x}, t)$ is the density distribution function in the α th direction, τ is the relaxation time which is related to the macroscopic kinetic viscosity of the fluid as $\nu = \frac{c^2}{3}(\tau - 0.5\Delta t)$. In this work, τ was set equal to 1 for the calculation stability. The lattice speed c is defined as the lattice spacing Δx divided by the time step Δt . The D3Q19 model (Huang et al., 2015) is employed with \mathbf{e}_{α} representing the 19 directional velocities. The equilibrium density distribution function $f_{\alpha}^{\text{eq}}(\mathbf{x}, t)$ is calculated as

$$f_{\alpha}^{\text{eq}}(\mathbf{x}, t) = w_{\alpha}\rho(\mathbf{x}, t) \left[1 + 3 \frac{\mathbf{e}_{\alpha} \cdot \mathbf{u}^{\text{eq}}}{c^2} + 4.5 \frac{(\mathbf{e}_{\alpha} \cdot \mathbf{u}^{\text{eq}})^2}{c^4} - 1.5 \frac{(\mathbf{u}^{\text{eq}})^2}{c^2} \right]. \quad (2)$$

For the D3Q19 model, $w_{\alpha} = 1/3$ ($\alpha = 0$), $w_{\alpha} = 1/18$ ($\alpha = 1-6$), $w_{\alpha} = 1/36$ ($\alpha = 7-18$). ρ is the macroscopic fluid density which is calculated by $\rho = \sum_{\alpha} f_{\alpha}$. The SC-LBM is based on the idea of representing the intermolecular interactions at the mesoscopic scale via a density dependent nearest-neighbor pseudopotential (Chen & Gary, 1998). In the model, the macroscopic velocity, which is represented by \mathbf{u}^{eq} , is calculated by the so-called velocity shift method:

$$\mathbf{u}^{\text{eq}} = \frac{\sum_{\alpha} f_{\alpha} \mathbf{e}_{\alpha}}{\rho} + \frac{\tau \mathbf{F}}{\rho}, \quad (3)$$

where \mathbf{F} is the interaction force which includes the fluid-fluid interaction force (i.e., the cohesive force or internal force, \mathbf{F}_{int}) and the fluid-solid interaction force (i.e., the adhesive force, \mathbf{F}_{ads}). \mathbf{F}_{int} is usually calculated with the following form of the pseudopotential:

$$\mathbf{F}_{\text{int}}(\mathbf{x}, t) = -G\psi(\mathbf{x}, t) \sum_{\alpha} w_{\alpha} \psi(\mathbf{x} + \mathbf{e}_{\alpha}\Delta t, t) \mathbf{e}_{\alpha}, \quad (4)$$

where ψ is the pseudopotential function. In this work, $\psi(\rho) = 1 - e^{-\rho}$ is employed. The separation of the liquid phase (ρ_l) and gas phase (ρ_g) is permitted when the interaction strength factor $G < -4$ for the above pseudopotential function (Shan & Chen, 1993). Throughout this work, G is set equal to -7 to avoid the gas phase condensation in front of the interface, which leads to a faster interface proceeding (Diotallevi et al., 2009). Under these settings, the coexist density of ρ_l and ρ_g are 3.27 and 0.04, respectively. This group of parameters are employed in the rest of the paper.

Moreover, the surface tension (σ) under the above settings is obtained through a series simulation of a liquid droplet surrounded by gas phase in a fully periodic domain without gravity. In each simulation, a spherical liquid droplet with a radius chosen from 25, 27, 29, 31, 33, and 35 lattices, respectively, is initialized in a periodic domain of $N_x \times N_y \times N_z = 101 \times 101 \times 101$ lattice unit. Then, the system is evolved into an equilibrium state. The reciprocal of the final droplet radius (r) and the half pressure difference ($\Delta P/2$) inside and outside the droplet are recorded. These data almost fall into a straight line, as shown in Figure 1. This finding agreed well with the Laplace law in the three dimensions, which states that $\Delta P/2 = \sigma/r$. With a linear fit, the σ in the system equals to 0.22871 in lattice unit.

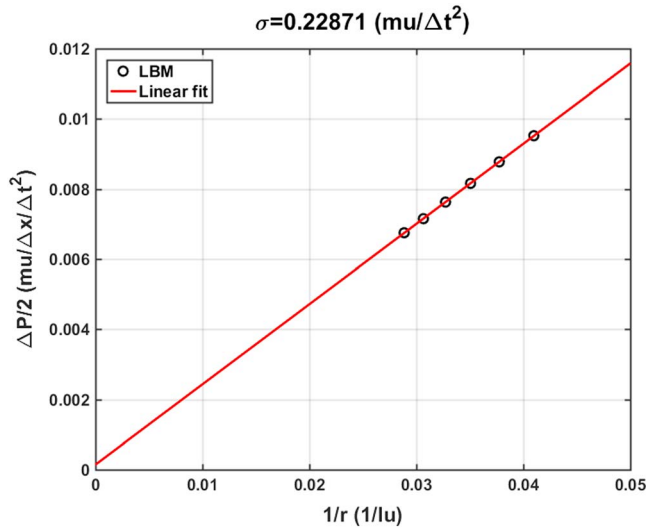


Figure 1. Half pressure difference ($\Delta P/2$) inside and outside of the droplet as a function of the reciprocal of the final droplet radius ($1/r$). A linear fit is plotted as a red line on the figure. LBM = lattice Boltzmann method.

A modified form of \mathbf{F}_{ads} is employed to better control the fluid density accumulation near the hydrophilic walls (Zheng et al., 2018):

$$\mathbf{F}_{ads}(\mathbf{x}, t) = -G\psi(\mathbf{x}, t)\sum_{\alpha}W_{\alpha}\psi(\beta\bar{\rho}_f)S(\mathbf{x} + \mathbf{e}_{\alpha}\Delta t, t)\mathbf{e}_{\alpha}, \quad (5)$$

where $S(\mathbf{x} + \mathbf{e}_{\alpha}\Delta t, t)$ is an index function, which equals to 1 for the solid nodes and 0 for the fluid nodes. The fictitious density of a wall node, that is, $\beta\bar{\rho}_f$, is determined by the averaging of the fluid density ($\bar{\rho}_f$) in its 26 neighboring nodes and a strength factor β . In the calculation, β is equal to 1 when $\bar{\rho}_f < 2\rho_g$ and equal to the setting value when $\bar{\rho}_f \geq 2\rho_g$. This newly proposed calculation of \mathbf{F}_{ads} inhibits the high interaction force between the solid nodes and the gas nodes and permits a better accuracy in the simulations with the solid nodes involved.

2.2. Determination of the Contact Angle on a Rough Surface

The different wetting conditions of the walls can be easily implemented by equation (5) with different values of β . It is similar to other schemes which set the fictitious wall density as a constant (Benzi et al., 2006; Fan et al., 2001; Huang et al., 2007). However, implementing the \mathbf{F}_{ads} by equation (5) eliminates the unphysical gas density condensation near the wall as introduced before. In most of the previous SC-LBM simulations, the wettability

of a wall was determined by measuring the contact angle of a liquid droplet on a flat surface (Benzi et al., 2006; Huang et al., 2007) or a liquid plug in a straight channel (Schaap et al., 2007) under certain settings. However, the real porous structure is composed of rough surfaces. As claimed by Wenzel (1936), the measured contact angle on a rough surface is different from that on a flat surface.

Here the influence of the wall roughness in the simulation was further analyzed with comparisons between the contact angles measured on a flat surface and a rough surface. The static contact angles of a liquid plug in a straight flat channel were first calculated by incorporating the proposed fluid-solid interaction with different values of β . In each simulation, a 40-lattice-long liquid plug was initialized in the middle of a channel with a size of $N_x \times N_y \times N_z = 100 \times 1 \times 42$ lattices. Other nodes in the channel were initialized as gas phase. A bounce-back boundary condition was employed for the top and bottom wall surfaces, and a periodic boundary condition was employed for other boundaries. The system was then evolved to an equilibrium state. The contact angle of each simulation was calculated based on the profile of the liquid plug. As shown in Figure 2, a wide range of static contact angles on the flat surface was obtained with different values of β .

Similarly, the static contact angles of a liquid droplet on a rough surface were calculated with different values of β . The calculation domain has a size of $N_x \times N_y \times N_z = 100 \times 1 \times 100$ lattices. It was divided by a diagonal line with the solid nodes in the left bottom half and the fluid nodes in the right top half. The wall thus has a standard stair-shaped surface. Similarly, the bounce-back boundary condition was employed for the wall nodes, and the periodic boundary condition was employed for the other boundaries. According to the definition given by Wenzel (1936), that is, the actual surface area divided by the geometric surface area, this surface has a roughness of $\sqrt{2}$. In each simulation, a semisphere liquid droplet with a radius of 14 lattices was initialized in the middle of the surface with the other liquid nodes occupied by the gas phase. The system was then evolved to an equilibrium state. Again, the contact angle of each simulation was calculated based on the equilibrium profile of the droplet. As shown in Figure 3, a wide range of static contact angles on the rough surface was obtained with different values of β . However, it should be noted that the contact angle obtained with the same value of β is different on the flat surface and the stair-shaped surface. For example, when β equals 2.2, the contact angles measured on the flat surface and the rough surface are 47.15° and 6.03° , respectively. This approximately obeys Wenzel's statement on a hydrophilic rough surface as $\cos(6.03^\circ) \approx \sqrt{2} \cos(47.15^\circ)$. The correspondence between β and the contact angle measured on a rough surface was used in the spontaneous imbibition simulation in the porous structures, which were composed of complex pore surfaces.

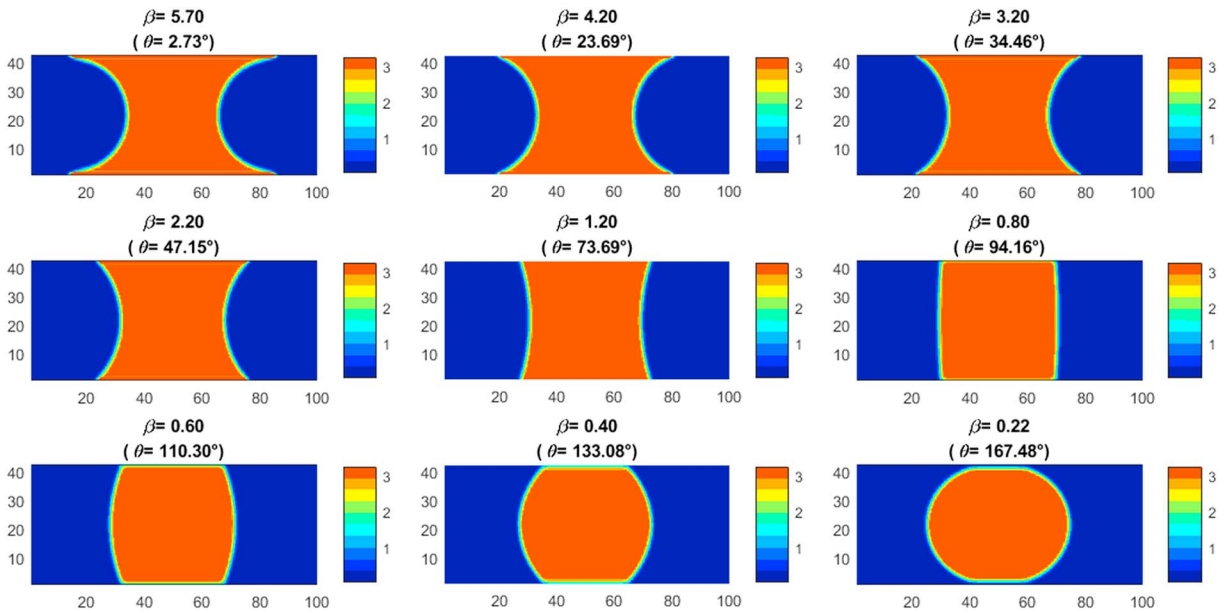


Figure 2. Contact angles calculated by the proposed method in a straight channel with different values of β .

2.3. Benchmark

The spontaneous imbibition process in a Y-shaped junction was simulated and compared with the experimental results (Sadjadi et al., 2015) to validate the accuracy of the proposed method. As shown in Figure 4a (image courtesy of Sadjadi et al., 2015), the Y-shaped junction was composed of a feeding channel with a length l_o and a width w_f , a wide branch with a width w_w , and a narrow branch with a width w_n . The channel has a constant height $\delta = 95\mu\text{m}$ and $l_o = 1,400\mu\text{m}$, $w_f = 53\mu\text{m}$, $w_n = 44\mu\text{m}$, and $w_w = 122\mu\text{m}$, which corresponds to the model B1 in the work of Sadjadi et al. (2015). A simplified model was employed in the simulation for the calculation efficiency, as illustrated in Figure 4b. The A–A cross-section geometry is shown right next to the model. The size of the simplified model was labeled in the figure with one lattice length representing $10\mu\text{m}$. The β was set equal to 5.7 to simulate a completely wetting wall surface. The bounce-back boundary condition was employed for the wall surfaces, and a periodic boundary condition was employed for the rest of the boundaries, as illustrated in Figure 4b. The lattice units were implemented in the calculation for simplicity. A detailed conversion to the physical units based on the Buckingham π theorem is given in Appendix A.

The meniscus split into two when it touched the branching point. At this time, the capillary pressure (negative value) provided by the meniscus was replaced by two abruptly decreasing capillary pressures, both of which were smaller than the capillary pressure before the meniscus split occurred. Meanwhile, the resistance force, which is still dominantly induced by the inlet channel, should be almost the same. The force equilibrium was broken in the system. As a result, an arrest time range can be observed for the meniscus in the wide channel, while the meniscus in the narrow channel showed a quick propagation just after the meniscus split. A detailed theoretical analysis of this phenomenon can be found in Sadjadi et al. (2015). The comparisons of the simulation and the experimental results are presented in Figure 5. As shown in Figure 5a, the simulated meniscus proceedings generally agreed well with the experimental results in the feeding channel and the two branches. A little discrepancy between the simulations and the experimental results can be observed when the meniscus split happens due to the simplified geometry. Figure 5b shows the menisci velocities in the two branches. As shown, the simulation results agreed well with the experiments. The general consistence between the simulation and the experiment validates that the proposed method can be safely employed to investigate the spontaneous imbibition behavior in the three-dimensional porous structures.

3. Results

The spontaneous imbibition behavior in a reproduced shale porous structure was simulated by the proposed method. The saturation data during the imbibition process were recorded. Moreover, the relative gas

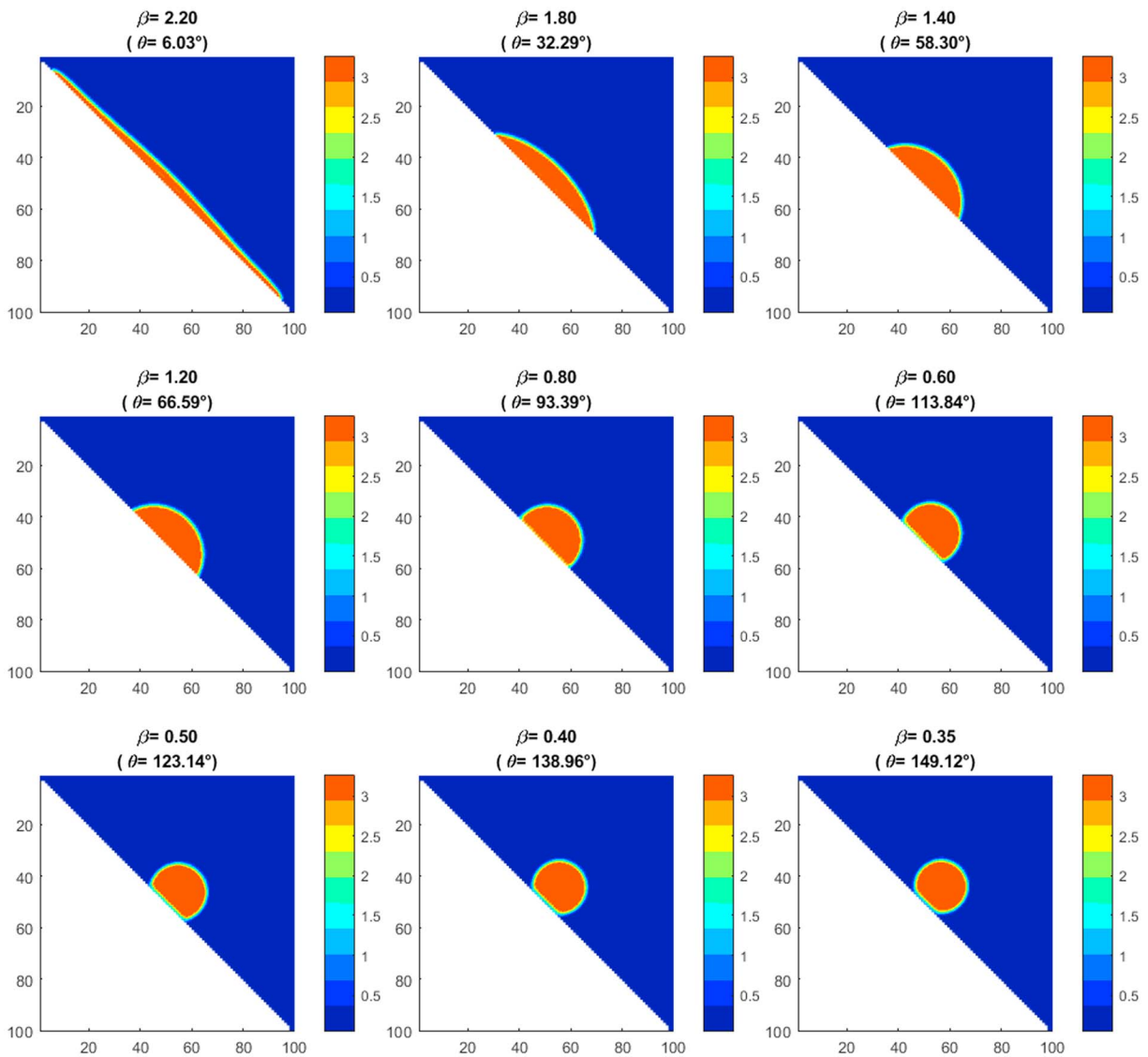


Figure 3. Contact angles calculated in a stair-shaped wall surface with different values of β .

permeability of the model during the spontaneous imbibition was calculated with consideration of the high-Knudsen effect (Zheng et al., 2017).

3.1. Reproduction of the Porous Structure Model of the Shale

Based on the previous classification of the porous structure in the shale (Zheng et al., 2017), a simple reconstruction procedure was employed to reproduce the porous structure model. Specifically, the three-dimensional digital shale porous structure was generated in three steps, which comprised the generation of intergranular pores, organic pores, and microfractures. The generated model has a size of $80 \times 160 \times 160$ voxels and comprises black and white voxels representing the pore space and the rock matrix, respectively.

A random sphere packing method (Ju, Huang, et al., 2017; Zheng et al., 2017) was used to generate the intergranular pores in the first step. Initially, the model was completely composed of black voxels. Then, white spheres, which represent the rock matrix, with a radius from 2 to 4 voxels were randomly inserted into the model until the porosity decreased to 30%. In this process, the white spheres were allowed to overlap with

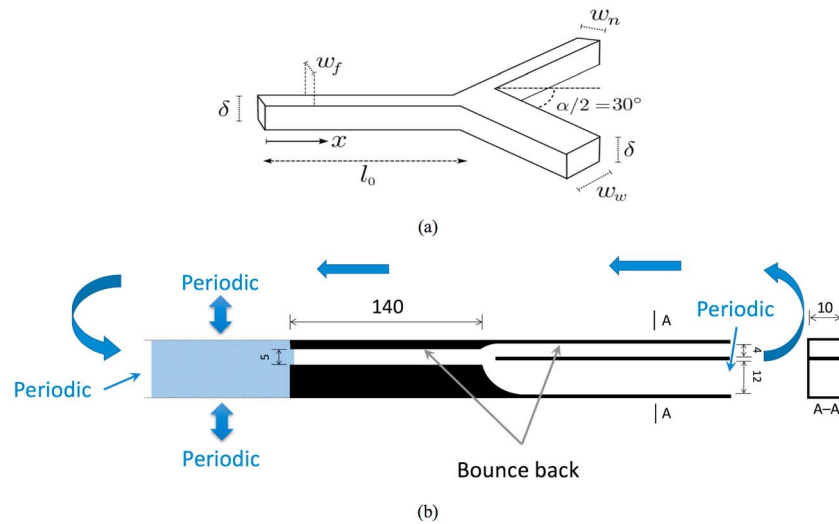


Figure 4. The Y-shaped junction model. (a) The model employed in the experimental work (image courtesy: Sadjadi et al., 2015), (b) the simplified three-dimensional geometrical model used in the simulation work (not to scale).

each other. After the generation step, the connected pores in the X direction were labeled and extracted, and the other isolated pores were eliminated. The effective porosity of the model was 26.98%.

A similar procedure was used to generate the organic pores in the second step. Black spheres, which represent the organic pores, with a radius from 3 to 5 voxels were randomly cast into the model generated in the first step. This was inspired by the observations that pores in the organic matters developed during the hydrocarbon thermal maturation usually show a nearly spherical shape. In the process, 400 organic pores were randomly cast into the model, which accounted for a porosity of 4.53%. Additionally, the organic pores are generally hydrophobic in contrast to the intergranular pores and microfractures. In particular, the pore surface position of these organic pores was recorded.

In the third step, a microfracture was cast into the model. The microcrack was defined by a random point $P(x_0, y_0, z_0)$ in the model, a random vector $\mathbf{B}(a, b, c)$ and its aperture H . The value of a , b , and c were random integers from $[-80, 80]$, $[-160, 160]$, and $[-160, 160]$, respectively. The value of H was random integers from 8 to 12. In the process, the voxels with a coordinator of (x, y, z) in the model, which met the criterion as defined by the following equation, were chosen as the microfracture voxels and set to black:

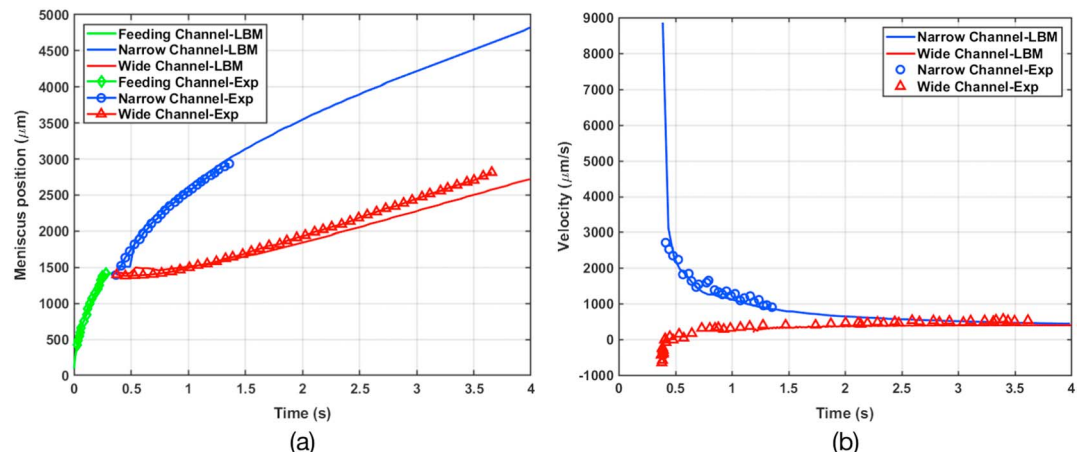


Figure 5. Comparison of the simulation and the experiment results of the spontaneous imbibition in a Y-shaped junction model. (a) Meniscus position along the imbibition. (b) Meniscus velocity after the split. LBM = lattice Boltzmann method.

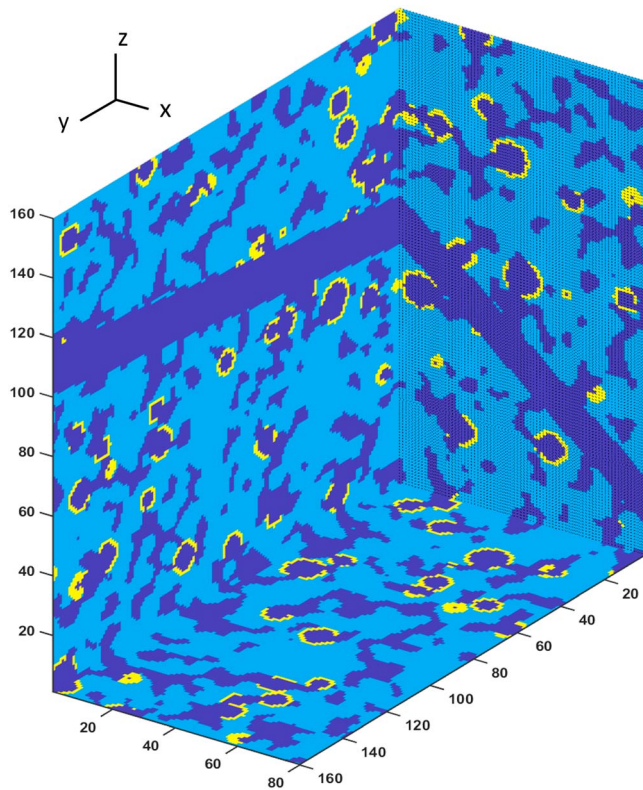


Figure 6. Reproduced shale porous structure model. The dark blue represents the pore space and the yellow represent the hydrophobic pore surface.

$$\frac{|a \times (x - x_0) + b \times (y - y_0) + c \times (z - z_0)|}{\sqrt{a^2 + b^2 + c^2}} \leq H/2. \quad (6)$$

The total porosity of the model is 36.61%. The three-dimensional appearance of the generated pore structure is shown in Figure 6 with the organic pore surface marked in yellow. It should be noted that the model generated here was at the nanoscale and with three types of pores compacted in. The spontaneous imbibition behavior in the model was simulated by the proposed method. However, a much larger scale, usually several kilometers, is involved in a real hydraulic fracturing shale gas well. A multiscale analysis would be helpful for bridging the gap between the nanoscale simulation and the real engineering applications. Nevertheless, further discussion of this kind of analysis is beyond the scope of this work.

3.2. Spontaneous Imbibition in the Complex Shale Porous Structure

The spontaneous imbibition behavior in the reproduced shale porous structure was simulated by the proposed SC-LBM in the lattice units. The three-dimensional liquid imbibition process and the density distribution in the slices of $Y = 10, 80,$ and 150 are shown in Figure 7. As illustrated in the upper row of Figure 7a, initially, a 15-lattice-long liquid plug was put in the left of the model with a 5-lattices intersection. The β value on the organic pore surface nodes (i.e., these yellow nodes in Figure 6) was set equal to 0.4 to simulate a hydrophobic surface ($\theta = 138.96^\circ$). In contrast, the β value on the other pore surface nodes was set equal to 2.2 to simulate a hydrophilic surface ($\theta = 6.06^\circ$). Similar to the benchmark case, the bounce-back boundary condition was employed for the pore surfaces, and a periodic boundary condition was employed for the rest of the model boundaries. The parameters used in the spontaneous imbibition simulation are listed in Table 1. Under the drive of the capillary forces provided by the hydrophilic pore surface, the liquid plug was gradually imbibed into the pore space of the model.

As shown, the liquid plug imbibed quicker in the larger fracture and slower in the smaller intergranular pores at the early stage. This is consistent with the LW equation, that is, $x^2 \propto \frac{D\sigma \cos(\theta)}{\mu} t$, where D is the characteristic pore size and μ is the viscosity. From the equation, one can derive that the liquid imbibe quicker in the larger pores. Due to the rapid spontaneous imbibition in the fracture, the tail interface of the liquid plug broken apart at the inlet surface, as shown in Figure 7b. Moreover, an additional meniscus formed in the fracture near the inlet which led to a backward capillary force. This backward force restrained the further propagation of the liquid fragment in the fracture, as shown in Figures 7b to 7e.

Additionally, the capillary force in the smaller pore is larger according to the Young-Laplace equation, that is, $P_c = \sigma \left(\frac{1}{R_1} + \frac{1}{R_2} \right)$. Thus, the liquid was gradually migrated from the larger size fracture to the smaller pores along with the imbibition. Along with this process, the liquid fragment in the fracture gradually decreased and resulted in a reopened channel, as shown in Figures 7e and 7f.

Moreover, the imbibition front bypassed most of the hydrophobic pores. As illustrated in Figure 7, most of the hydrophobic pores, whose surface nodes marked in black in the density distribution slices, remained gas-filled. However, it should be noted that the liquid could be pushed into these hydrophobic pores, as shown in the upper left corner of $Y = 80$ and 150 slices in Figure 7f. This phenomenon only appeared when the P_c values induced by the neighbor hydrophilic pores were all larger than the repelling pressure provided by the hydrophobic pore. As shown, the filled hydrophobic pores were characterized by a large open surface which results in a small repelling capillary pressure.

Moreover, the imbibition front bypassed most of the hydrophobic pores. As illustrated in Figure 7, most of the hydrophobic pores, whose surface nodes marked in black in the density distribution slices, remained gas-filled. However, it should be noted that the liquid could be pushed into these hydrophobic pores, as shown in the upper left corner of $Y = 80$ and 150 slices in Figure 7f. This phenomenon only appeared when the P_c values induced by the neighbor hydrophilic pores were all larger than the repelling pressure provided by the hydrophobic pore. As shown, the filled hydrophobic pores were characterized by a large open surface which results in a small repelling capillary pressure.

3.3. Saturation and Permeability Along With the Imbibition

The water saturation of the model (S_w) was recorded along with the spontaneous imbibition. Moreover, in order to analyze the influence of the spontaneous imbibition on the transport property of the model, a

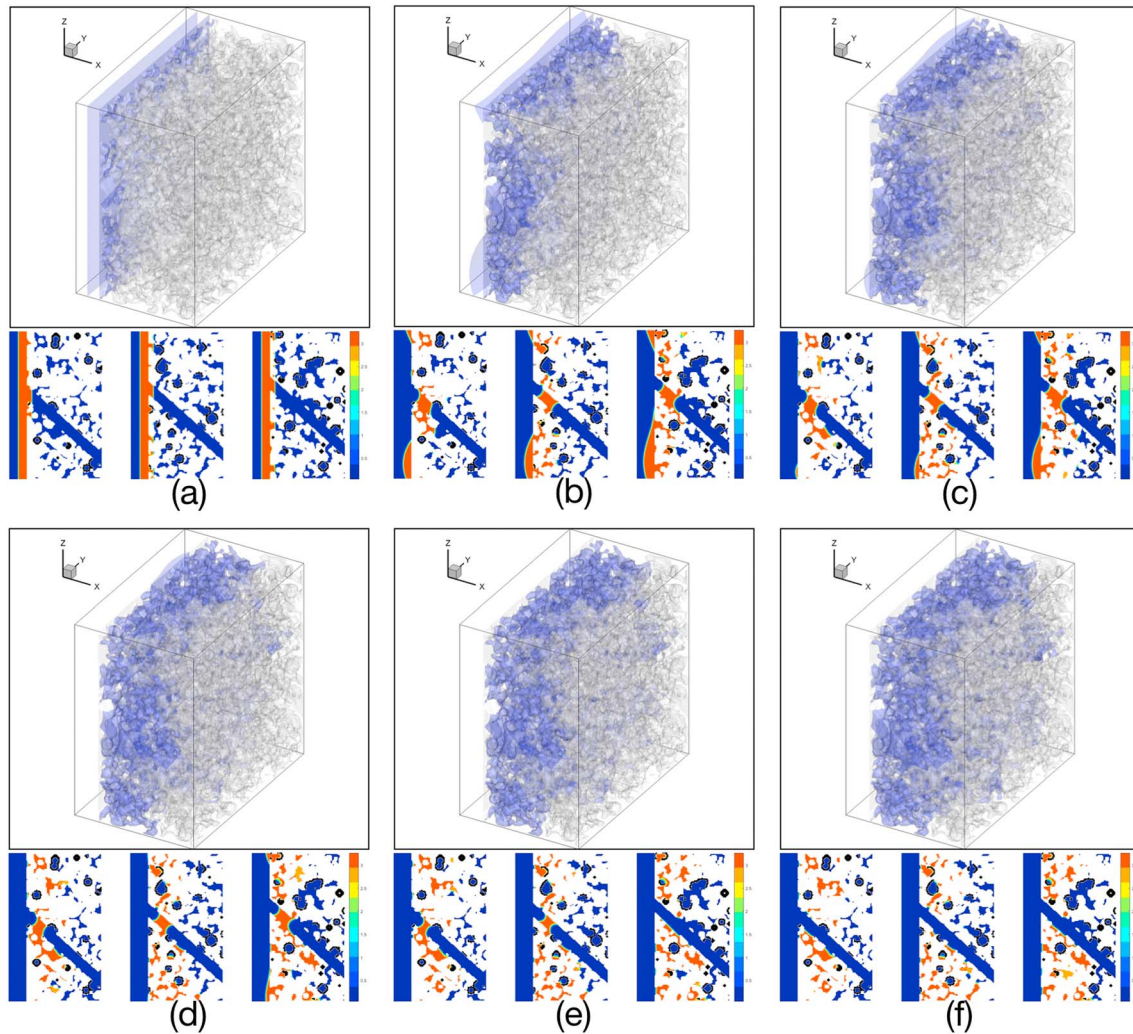


Figure 7. Simulated spontaneous imbibition behavior in the reproduced shale porous structure. The upper row in each figure is the three-dimensional appearance of the spontaneous imbibition behavior at different time steps, where the blue represents the imbibed liquid and the gray represent the pore space. The lower row in each figure is the density distribution in the slices of $Y = 10, 80,$ and 150 . In each slice, the hydrophobic pore surface nodes are denoted by black dots. (a) is the imbibition at initial stage, and (b)–(f) is the imbibition at the time steps of $1 \times 10^4, 2 \times 10^4, 3 \times 10^4, 4 \times 10^4,$ and 5×10^4 , respectively.

single phase LBM (Zheng et al., 2018) was employed to calculate the apparent gas permeability (k_{ga}) of the model. Since nanoscale pores are dominant in a shale matrix, the high Knudsen effect (Kn) was involved in the calculation of the gas flow behavior in these pores. In the calculation, a pressure gradient along the X direction was applied on the sample to drive the gas flow. The calculation terminated when the average

velocity was nearly unchanged: $\left| \frac{\overline{U}_x - \overline{U}'_x}{\overline{U}_x} \right| < 10^{-4}$, where \overline{U}_x and \overline{U}'_x are the average velocities in the current

and previous iteration time step. Subsequently, the k_{ga} was calculated based on the velocity data according to Darcy's law. The parameters used in the simulation are listed in Table 2. The k_{ga} of the reproduced model without the spontaneous imbibition involved is equal to 8.74×10^{-2} mD.

In the calculation of k_{ga} during the spontaneous imbibition, the pores occupied by the liquid phase were treated as *walls*, and the other pores were treated as the gas flow channels. At the beginning of the spontaneous imbibition, the liquid plug had five lattices overlap with the model, leading to all the pores with X coordinate less than or equal to 5 being

Table 1
Parameters Used in the Spontaneous Imbibition Simulation

Parameter	Value
Domain size (lattices)	$100 \times 160 \times 160$
Model size (lattices)	$80 \times 160 \times 160$
β for hydrophilic pores	2.2
β for hydrophobic pores	0.4
Initial liquid plug length (lattices)	15

Table 2
Parameters Used in the k_{ga} Calculation

Parameter	Value
Domain size (lattices)	$80 \times 160 \times 160$
Lattice length, dx (m)	1×10^{-8}
Temperature, T (K)	380
Gas constant, R ($J \cdot mol^{-1} \cdot K^{-1}$)	8.314
Molar Mass, M (kg/mol)	0.016
Gas density, ρ (kg/m^3)	15.19
Gas pressure, P (MPa)	3
Press gradient, $\nabla_x P$ (MPa/m)	-1
Dynamic viscosity, μ ($kg \cdot m^{-1} \cdot s^{-1}$)	1.4×10^{-5}

filled with the liquid phase. As expected, the k_{ga} of the model at this stage was zero. Due to the pore size heterogeneity, the liquid imbibition front was nonuniform. Along with the spontaneous imbibition, the fracture was first reopened resulting in a rapid k_{ga} increase. Figure 8 shows the S_w and k_{ga} of the model along with the spontaneous imbibition. As shown, the S_w of the model increased quickly at the initial stage. This corresponds to the quick imbibition into the fracture and hydrophilic pores near the left surface of the model. During the process, all the liquid plug was imbibed into the pore space of the model, which corresponding to a saturation of 41.06%. At the time step of 3.9×10^4 , the model was reopened in the X direction, which led to the rapid increase of k_{ga} . At the time step of 7.50×10^4 , the S_w and k_{ga} were nearly unchanged. At this time, the k_{ga} of

the model equals 7.51×10^{-2} mD, which is 85.86% of the model permeability without the liquid imbibition involved. The great recovery of the model permeability along the spontaneous imbibition can be considered to be a direct evidence of the relatively high gas production after the shut-in operation in some shale gas wells.

4. Discussion

A direct pore-scale simulation of the spontaneous imbibition behavior in the reproduced shale porous structure was presented in this work. Moreover, the S_w and k_{ga} of the model along with the spontaneous imbibition were calculated. This detailed investigation of the spontaneous imbibition behavior and its influences on the model permeability allow one to better understand the correlations between the pore scale spontaneous imbibition behavior and the engineering observed phenomena, such as the low flowback rate and the relatively high gas production after the shut-in operation.

Given the information gained from the simulation, we can partially answer the two main concerns related to the low flowback rate in a shale gas reservoir stimulation. For the first concern, the hydrophilic pores in the shale matrix provide the driving force and storage space for holding the fracturing fluid. As claimed by Engelder et al. (2014), the pore space in the deep underground shale reservoir is enough to host the fracturing fluid. The nanoscale pores in the shale lead to large capillary forces. Under the assumption that the capillary force is the main driving force, the fracturing fluid tends to migrate to the smaller pores in the shale reservoir. Following this assumption, the tendency of the fracturing fluid to migrate to the nanoscale small pores in the shale matrix reduces the potential of the upward migration to the shallow water aquifers through a larger natural connectivity.

For the second concern, the recovery of k_{ga} to 85.86% of its dry state suggests that the gas production ability of the reservoir is greatly recovered after the shut-in operation. Unlike the tight sandstone, which is composed of relatively uniform small pores (Sakhaee-Pour & Bryant, 2014), the shale is composed of not only geometrical complexity but also mixed wettability pores (Loucks et al., 2009). The pore size and wettability heterogeneity causes the nonuniform propagation of the imbibition front (Bennion & Thomas, 2005). As illustrated in the simulation, the reopening of the fracture and large pores lead to a large portion of the k_{ga} recovery. This should be one of the main reasons that a shale gas reservoir is less influenced by the water blockage damage after the shut-in operation.

However, some limitations of the current method should be noted. First, a nanoscale model was used in this work. A much larger scale (usually several kilometers) is involved in a real engineering application. A multiscale analysis would be helpful for this kind of study. Moreover, the in situ condition, which characterized by high pore pressure, high geostress, high temperature, and low initial water saturation (Engelder et al., 2014; Gao & Hu, 2016a; Singh, 2016), cannot be fully covered by the current method. A coupled spontaneous imbibition simulation involving both mechanical and hydraulic effects is certainly important for understanding the related fluid migration pattern and the shale gas production. In addition, a

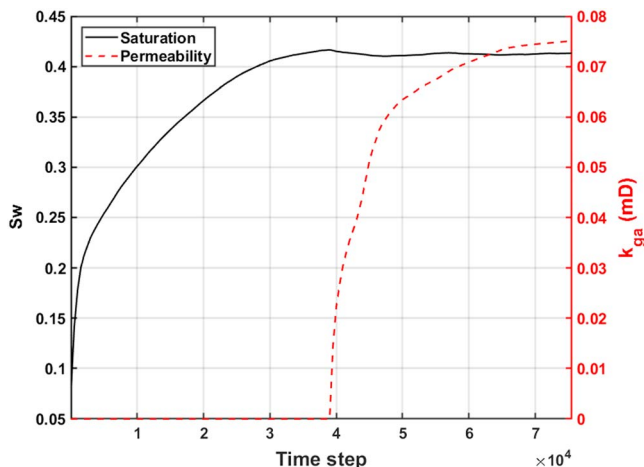


Figure 8. The S_w and k_{ga} of the model along with the spontaneous imbibition.

reproduced porous structure was employed with a focus on the pore space. As a result, it has a porosity much larger than the in situ tested porosity. Although the focused ion beam scanning electron microscope or nano-CT images of the nanoscale shale porous structure are available, they usually focus on a small region with a particular pore type in each test (Kelly et al., 2016). Alternatively, the reproduction of the complex shale porous structure gives an opportunity to investigate the imbibition in the pores space composed of the different types of pores. Although primary, this work provides a novel way to directly investigate the spontaneous imbibition in the three-dimensional complex pore structures.

5. Conclusions

A modified SC-LBM is proposed in this work to simulate the spontaneous imbibition behavior in a reproduced three-dimensional complex shale porous structure. The reproduced model is composed of intergranular pores, organic pores, and microfractures, which not only contains a complex morphology but also shows mixed wettability. With modification of incorporating the fluid-solid interaction force, the proposed method can eliminate the unphysical fluid density condensation near the wall. Moreover, the particular fluid-solid interaction strength factors β are determined on a rough wall, which is more applicable in simulating the spontaneous imbibition in complex porous structures.

The simulation results showed that (1) due to the capillary force provided by the hydrophilic pore surface, the fluid was gradually imbibed into the pore space. Due to the pore size and wettability heterogeneity, a nonuniform interface propagation was observed in the simulation. (2) The calculation of the k_{ga} along with the spontaneous imbibition showed that the k_{ga} rapidly increased along with the reopening in the larger pores. A recovery of the k_{ga} to 85.86% of its initial state was observed along with the spontaneous imbibition. These two findings may show their significance in interpreting the engineering observed phenomena. First, the spontaneous imbibition should be one of the main reasons for low flowback rate in a shale gas production well after hydraulic fracturing. Second, the great recovery of the k_{ga} along with the spontaneous imbibition may be responsible for the relatively high productivity after the shut-in operation in many shale gas wells.

Appendix A

A simple procedure based on the Buckingham π theorem is used to convert the lattice unit system to the physical unit system. In most of the literature employing LBM, the lattice unit system was used in the calculations for implementation convenience. Several works have presented clear conversion procedure for both single phase (Feng et al., 2007) and multiphase flow simulations (Schaap et al., 2007). However, certain difficulties arise when employing the one component two phase SC-LBM. In a typical SC-LBM simulation, the two phases coexist densities (ρ_g and ρ_l) and the surface tension (σ) are simultaneously determined by the interaction strength factor (G), which cannot be tuned independently. This leads to the difficulties in keeping all the similarity requirements between the simulation and the physical prototype. Although few attempts were proposed to address this problem (Li & Luo, 2013; Sbragaglia et al., 2007), the introduced additional parameters made the conversion more complicated. Here we introduce a simple procedure to accomplish the mapping of the simulation of spontaneous imbibition to the real physical case.

For a spontaneous imbibition case, capillary forces and viscous forces are the two dominate forces in the system (Gruener et al., 2012; Sadjadi et al., 2015). Moreover, away from the initial stage, small Reynolds number ($Re = \frac{\rho V L}{\mu}$) and Weber number ($We = \frac{\rho V^2 L}{\sigma}$) characterize the system (Fries & Dreyer, 2008), which indicates that the inertial forces can be safely neglected. Under this assumption, a general relationship between the spontaneous imbibition velocity and other variables in the system can be expressed as

$$V = f(\rho, H, L, \mu, \sigma, \theta), \quad (A1)$$

where ρ is the imbibed fluid density, V is the spontaneous imbibition velocity, H and L are two characteristic lengths of the imbibition cross-section, μ and σ are the viscosity and surface tension of the imbibed fluid, respectively, θ is the contact angle of the imbibed fluid on the pore surface. In the equation, there are seven variables involved with three reference dimensions. According to the Buckingham π theorem (Munson et al.,

2013), four independent Π terms are required to fully describe the spontaneous imbibition process. Thus, equation (A1) can be rearranged into

$$\Pi_1 = \phi(\Pi_2, \Pi_3, \Pi_4). \quad (\text{A2})$$

Here we choose Π_1 as capillary number, that is, $\Pi_1 = C_a = \frac{\mu V}{\sigma}$, Π_2 equal to the geometrical aspect ratio as $\Pi_2 = \frac{H}{L}$, Π_3 as the contact angle, that is, $\Pi_3 = \cos(\theta)$, and Π_4 as the Reynolds number, that is, $\Pi_4 = R_e = \frac{\rho V L}{\mu}$. A corresponding relationship can be written for the simulation case:

$$\Pi_{1l} = \phi(\Pi_{2l}, \Pi_{3l}, \Pi_{4l}). \quad (\text{A3})$$

Here the subscript l represent the lattice unit system in the simulation. The form of equations (A2) and (A3) will be the same as the same phenomenon is involved both in the simulation and the real case. As noted before, the spontaneous imbibition phenomenon was characterized by small R_e away from the initial stage. Then, without considering the inertia force, the similarity requirement of Π_4 and Π_{4l} can be safely ignored. As a result, if the Π_{2l} and Π_{3l} in the simulation are set as $\Pi_{2l} = \Pi_2$ and $\Pi_{3l} = \Pi_3$, then $\Pi_{1l} = \Pi_1$.

Take the spontaneous imbibition in the Y-shaped channel as an example. In the simulation, we scaled the Y-shaped channel into a simplified geometry with one feeding channel and two branches. The lattice length (dx) in the simplified model represents a length of $10 \mu\text{m}$. The value of Π_{2l} and Π_2 were almost the same. A complete wetting surface was simulated to make sure $\Pi_{3l} = \Pi_3$. With these settings, the value of Π_{1l} should be equal to Π_1 , as $\frac{\mu_l V_l}{\sigma_l} = \frac{\mu V}{\sigma}$. In the simulation $\frac{\mu_l}{\sigma_l} = 2.383$ and in the experiment $\frac{\mu}{\sigma} = 2.333 \text{ (m/s)}^{-1}$, which results in $V = 1.021 V_l \text{ (m/s)}$. In other words, by multiplying the velocity in the simulation by a factor of 1.021, one can get the velocity in the experiment. Moreover, with dx equals to $10 \mu\text{m}$, the iteration step (dt) in the simulation represents a time interval of $10.21 \mu\text{s}$. With this method, one can easily convert the lattice units in the simulation into physical units in the real cases.

Acknowledgments

This work is financially supported by the State Key Research Development Program of China (grant 2016YFC0600705), National Major Project for Science and Technology of China (2017ZX05003-006), National Natural Science Foundation of China (grant U1562217, 51674251, 51727807), the Fundamental Research Funds for the Central Universities (00/800015NM), and China Postdoctoral Science Foundation (grant 2017M610877). The data for this paper can be obtained from <https://figshare.com/s/89ab23125659714fe91d>.

References

- Abbasi, M. A., Ezulike, D. O., Dehghanpour, H., & Hawkes, R. V. (2014). A comparative study of flowback rate and pressure transient behavior in multifractured horizontal wells completed in tight gas and oil reservoirs. *Journal of Natural Gas Science and Engineering*, *17*, 82–93. <https://doi.org/10.1016/j.jngse.2013.12.007>
- Aidun, C. K., & Clausen, J. R. (2010). Lattice-Boltzmann method for complex flows. *Annual Review of Fluid Mechanics*, *42*(1), 439–472. <https://doi.org/10.1146/annurev-fluid-121108-145519>
- Akbarabadi, M., & Piri, M. (2014). Nanotomography of the spontaneous imbibition in shale. Paper presented at the Unconventional Resources Technology Conference, Denver, Colorado, USA.
- Andrew, M., Bijeljic, B., & Blunt, M. J. (2014). Pore-scale contact angle measurements at reservoir conditions using X-ray microtomography. *Advances in Water Resources*, *68*, 24–31. <https://doi.org/10.1016/j.advwatres.2014.02.014>
- Arshadi, M., Zolfaghari, A., Piri, M., Al-Muntasheri, G. A., & Sayed, M. (2017). The effect of deformation on two-phase flow through proppant-packed fractured shale samples: A micro-scale experimental investigation. *Advances in Water Resources*, *105*, 108–131. <https://doi.org/10.1016/j.advwatres.2017.04.022>
- Bennion, D. B., & Thomas, F. B. (2005). Formation damage issues impacting the productivity of low permeability, low initial water saturation gas producing formations. *Journal of Energy Resources Technology*, *127*(3), 240–247. <https://doi.org/10.1115/1.1937420>
- Benzi, R., Biferale, L., Sbragaglia, M., Succi, S., & Toschi, F. (2006). Mesoscopic modeling of a two-phase flow in the presence of boundaries: The contact angle. *Physical Review E*, *74*(2), 021509. <https://doi.org/10.1103/physreve.74.021509>
- Bertoncello, A., Wallace, J., Blyton, C., Honarpour, M., & Kabir, C. S. (2014). Imbibition and water blockage in unconventional reservoirs: Well-management implications during flowback and early production. *SPE Reservoir Evaluation & Engineering*, *17*(04), 497–506. <https://doi.org/10.2118/167698-ms>
- Birdsell, D. T., Rajaram, H., Dempsey, D., & Viswanathan, H. S. (2015). Hydraulic fracturing fluid migration in the subsurface: A review and expanded modeling results. *Water Resources Research*, *51*, 7159–7188. <https://doi.org/10.1002/2015wr017810>
- Blunt, M. J., Bijeljic, B., Dong, H., Gharbi, O., Iglauer, S., Mostaghimi, P., et al. (2013). Pore-scale imaging and modelling. *Advances in Water Resources*, *51*, 197–216. <https://doi.org/10.1016/j.advwatres.2012.03.003>
- Cai, J., & Yu, B. (2011). A discussion of the effect of tortuosity on the capillary imbibition in porous media. *Transport in Porous Media*, *89*(2), 251–263. <https://doi.org/10.1007/s11242-011-9767-0>
- Chakraborty, N., Karpyn, Z. T., Liu, S., & Yoon, H. (2017). Permeability evolution of shale during spontaneous imbibition. *Journal of Natural Gas Science and Engineering*, *38*, 590–596. <https://doi.org/10.1016/j.jngse.2016.12.031>
- Chalmers, G. R., Bustin, R. M., & Power, I. M. (2012). Characterization of gas shale pore systems by porosimetry, pycnometry, surface area, and field emission scanning electron microscopy/transmission electron microscopy image analyses: Examples from the Barnett, Woodford, Haynesville, Marcellus, and Doig units. *AAPG Bulletin*, *96*(6), 1099–1119. <https://doi.org/10.1306/10171111052>
- Chen, S., & Gary, D. D. (1998). Lattice Boltzmann method for fluid flows. *Annual Review of Fluid Mechanics*, *30*(1), 329–364. <https://doi.org/10.1146/annurev.fluid.30.1.329>
- Cheng, Y. (2012). Impact of water dynamics in fractures on the performance of hydraulically fractured wells in gas shale reservoirs. *Journal of Canadian Petroleum Technology*, *51*(02), 143–151. <https://doi.org/10.2118/127863-pa>

- Clarkson, C. R., Haghshenas, B., Ghanizadeh, A., Qanbari, F., Williams-Kovacs, J. D., Riazi, N., et al. (2016). Nanopores to megafractures: Current challenges and methods for shale gas reservoir and hydraulic fracture characterization. *Journal of Natural Gas Science and Engineering*, *31*, 612–657. <https://doi.org/10.1016/j.jngse.2016.01.041>
- Curtis, M. E., Ambrose, R. J., & Sondergeld, C. H. (2010). Structural characterization of gas shales on the micro- and nano-scales. Paper presented at the Canadian Unconventional Resources and International Petroleum Conference, Calgary, Alberta, Canada.
- De Maio, A., Palpacelli, S., & Succi, S. (2011). A new boundary condition for three-dimensional lattice Boltzmann simulations of capillary filling in rough micro-channels. *Communications in Computational Physics*, *9*(5), 1284–1292. <https://doi.org/10.4208/cicp.141009.2411105>
- Dehghanpour, H., Lan, Q., Saeed, Y., Fei, H., & Qi, Z. (2013). Spontaneous imbibition of brine and oil in gas shales: Effect of water adsorption and resulting microfractures. *Energy & Fuels*, *27*(6), 3039–3049. <https://doi.org/10.1021/ef4002814>
- Dehghanpour, H., Zubair, H. A., Chhabra, A., & Ullah, A. (2012). Liquid intake of organic shales. *Energy & Fuels*, *26*(9), 5750–5758. <https://doi.org/10.1021/ef3009794>
- Desbois, G., Urai, J. L., Kukla, P. A., Konstanty, J., & Baerle, C. (2011). High-resolution 3D fabric and porosity model in a tight gas sandstone reservoir: A new approach to investigate microstructures from mm- to nm-scale combining argon beam cross-sectioning and SEM imaging. *Journal of Petroleum Science and Engineering*, *78*(2), 243–257. <https://doi.org/10.1016/j.petrol.2011.06.004>
- Diotallevi, F., Biferale, L., Chibbaro, S., Pontrelli, G., Toschi, F., & Succi, S. (2009). Lattice Boltzmann simulations of capillary filling: Finite vapour density effects. *The European Physical Journal Special Topics*, *171*(1), 237–243. <https://doi.org/10.1140/epjst/e2009-01034-6>
- Engelder, T. (2012). Capillary tension and imbibition sequester frack fluid in Marcellus gas shale. *Proceedings of the National Academy of Sciences of the United States of America*, *109*(52), E3625–E3625. <https://doi.org/10.1073/pnas.1216133110>
- Engelder, T., Cathles, L. M., & Bryndzia, L. T. (2014). The fate of residual treatment water in gas shale. *Journal of Unconventional Oil and Gas Resources*, *7*, 33–48. <https://doi.org/10.1016/j.juogr.2014.03.002>
- Fakcharoenphol, P., Torcuk, M. A., Wallace, J., Bertonecello, A., Kazemi, H., Wu, Y.-S., & Honarpour, M. (2013). Managing shut-in time to enhance gas flow rate in hydraulic fractured shale reservoirs: A simulation study. Paper presented at the SPE Annual Technical Conference and Exhibition, New Orleans, Louisiana, USA.
- Fan, L., Fang, H., & Lin, Z. (2001). Simulation of contact line dynamics in a two-dimensional capillary tube by the lattice Boltzmann model. *Physical Review E*, *63*(5), 051603. <https://doi.org/10.1103/physreve.63.051603>
- Feng, Y. T., Han, K., & Owen, D. R. J. (2007). Coupled lattice Boltzmann method and discrete element modelling of particle transport in turbulent fluid flows: Computational issues. *International Journal for Numerical Methods in Engineering*, *72*(9), 1111–1134. <https://doi.org/10.1002/nme.2114>
- Fries, N., & Dreyer, M. (2008). The transition from inertial to viscous flow in capillary rise. *Journal of Colloid and Interface Science*, *327*(1), 125–128. <https://doi.org/10.1016/j.jcis.2008.08.018>
- Gao, Z., & Hu, Q. (2016a). Initial water saturation and imbibition fluid affect spontaneous imbibition into Barnett shale samples. *Journal of Natural Gas Science and Engineering*, *34*, 541–551. <https://doi.org/10.1016/j.jngse.2016.07.038>
- Gao, Z., & Hu, Q. (2016b). Wettability of Mississippian Barnett Shale samples at different depths: Investigations from directional spontaneous imbibition. *AAPG Bulletin*, *100*(1), 101–114. <https://doi.org/10.1306/09141514095>
- Ghanbari, E., Abbasi, M. A., Dehghanpour, H., & Bearinger, D. (2013). Flowback volumetric and chemical analysis for evaluating load recovery and its impact on early-time production. Paper presented at the SPE Unconventional Resources Conference Canada, Calgary, Alberta, Canada.
- Ghanbari, E., & Dehghanpour, H. (2015). Impact of rock fabric on water imbibition and salt diffusion in gas shales. *International Journal of Coal Geology*, *138*, 55–67. <https://doi.org/10.1016/j.coal.2014.11.003>
- Ghanbari, E., & Dehghanpour, H. (2016). The fate of fracturing water: A field and simulation study. *Fuel*, *163*, 282–294. <https://doi.org/10.1016/j.fuel.2015.09.040>
- Gruener, S., & Huber, P. (2011). Imbibition in mesoporous silica: Rheological concepts and experiments on water and a liquid crystal. *Journal of Physics: Condensed Matter*, *23*(18), 184109. <https://doi.org/10.1088/0953-8984/23/18/184109>
- Gruener, S., Sadjadi, Z., Hermes, H. E., Kityk, A. V., Knorr, K., Egelhaaf, S. U., et al. (2012). Anomalous front broadening during spontaneous imbibition in a matrix with elongated pores. *Proceedings of the National Academy of Sciences of the United States of America*, *109*(26), 10,245–10,250. <https://doi.org/10.1073/pnas.1119352109>
- Houben, M. E., Urai, J. L., & Desbois, G. (2013). Pore morphology and distribution in the Shaly facies of Opalinus Clay (Mont Terri, Switzerland): Insights from representative 2D BIB–SEM investigations on mm to nm scale. *Applied Clay Science*, *71*(1), 82–97. <https://doi.org/10.1016/j.clay.2012.11.006>
- Hu, Q., Ewing, R. P., & Rowe, H. D. (2015). Low nanopore connectivity limits gas production in Barnett formation. *Journal of Geophysical Research: Solid Earth*, *120*, 8073–8087. <https://doi.org/10.1002/2015JB012103>
- Huang, H., Sukop, M. C., & Lu, X. Y. (2015). *Multiphase lattice Boltzmann methods: Theory and application*. Oxford, UK: Wiley-Blackwell. <https://doi.org/10.1002/9781118971451>
- Huang, H., Thorne, D. T., Schaap, M. G., & Sukop, M. C. (2007). Proposed approximation for contact angles in Shan-and-Chen-type multi-component multiphase lattice Boltzmann models. *Physical Review E*, *76*(6), 75–80. <https://doi.org/10.1103/physreve.76.066701>
- Ju, Y., Gong, W., Chang, C., Xie, H., Xie, L., & Liu, P. (2017). Three-dimensional characterisation of multi-scale structures of the Silurian Longmaxi shale using focused ion beam-scanning electron microscopy and reconstruction technology. *Journal of Natural Gas Science and Engineering*, *46*, 26–37. <https://doi.org/10.1016/j.jngse.2017.07.015>
- Ju, Y., Huang, Y., Zheng, J., Qian, X., Xie, H., & Zhao, X. (2017). Multi-thread parallel algorithm for reconstructing 3D large-scale porous structures. *Computers & Geosciences*, *101*, 10–20. <https://doi.org/10.1016/j.cageo.2017.01.003>
- Kelly, S., El-Sobky, H., Torres-Verdin, C., & Balhoff, M. T. (2016). Assessing the utility of FIB-SEM images for shale digital rock physics. *Advances in Water Resources*, *95*, 302–316. <https://doi.org/10.1016/j.advwatres.2015.06.010>
- Lan, Q., Xu, M., Binazadeh, M., Dehghanpour, H., & Wood, J. M. (2015). A comparative investigation of shale wettability: The significance of pore connectivity. *Journal of Natural Gas Science and Engineering*, *27*, 1174–1188. <https://doi.org/10.1016/j.jngse.2015.09.064>
- Li, Q., & Luo, K. H. (2013). Achieving tunable surface tension in the pseudopotential lattice Boltzmann modeling of multiphase flows. *Physical Review E*, *88*(5), 053307. <https://doi.org/10.1103/physreve.88.053307>
- Li, Q., Luo, K. H., Kang, Q. J., He, Y. L., Chen, Q., & Liu, Q. (2016). Lattice Boltzmann methods for multiphase flow and phase-change heat transfer. *Progress in Energy and Combustion Science*, *52*, 62–105. <https://doi.org/10.1016/j.pecs.2015.10.001>
- Liu, H.-H., Lai, B., & Chen, J. (2016). Unconventional spontaneous imbibition into shale matrix: Theory and a methodology to determine relevant parameters. *Transport in Porous Media*, *111*(1), 41–57. <https://doi.org/10.1007/s11242-015-0580-z>
- Liu, H. H., Ranjith, P. G., Georgi, D. T., & Lai, B. T. (2016). Some key technical issues in modelling of gas transport process in shales: A review. *Geomechanics and Geophysics for Geo-Energy and Geo-Resources*, *2*(4), 231–243. <https://doi.org/10.1007/s40948-016-0031-5>

- Loucks, R. G., Reed, R. M., Ruppel, S. C., & Hammes, U. (2012). Spectrum of pore types and networks in mudrocks and a descriptive classification for matrix-related mudrock pores. *AAPG Bulletin*, *96*(6), 1071–1098. <https://doi.org/10.1306/08171111061>
- Loucks, R. G., Reed, R. M., Ruppel, S. C., & Jarvie, D. M. (2009). Morphology, genesis, and distribution of nanometer-scale pores in siliceous mudstones of the Mississippian Barnett Shale. *Journal of Sedimentary Research*, *79*(12), 848–861. <https://doi.org/10.2110/jsr.2009.092>
- Lucas, R. (1918). Ueber das Zeitgesetz des kapillaren Aufstiegs von Flüssigkeiten. *Kolloid Zeitschrift*, *23*(1), 15–22. <https://doi.org/10.1007/bf01461107>
- Munson, B. R., Okiishi, T. H., Huebsch, W. W., & Rothmayer, A. P. (2013). *Fundamentals of fluid mechanics*. Hoboken, NJ: John Wiley.
- Nia, S. F., Dasani, D., Tsotsis, T. T., & Jessen, K. (2016). An integrated approach for the characterization of shales and other unconventional resource materials. *Industrial & Engineering Chemistry Research*, *55*(12), 3718–3728. <https://doi.org/10.1021/acs.iecr.5b04761>
- O'Malley, D., Karra, S., Currier, R. P., Makedonska, N., Hyman, J. D., & Viswanathan, H. S. (2016). Where does water go during hydraulic fracturing? *Ground Water*, *54*(4), 488–497. <https://doi.org/10.1111/gwat.12380>
- Piri, M., & Blunt, M. J. (2005). Three-dimensional mixed-wet random pore-scale network modeling of two- and three-phase flow in porous media. I. Model description. *Physical Review E*, *71*(2), 026301. <https://doi.org/10.1103/PhysRevE.71.026301>
- Raiskinmäki, P., Shakib-Manesh, A., Jäsberg, A., Koponen, A., Merikoski, J., & Timonen, J. (2002). Lattice-Boltzmann simulation of capillary rise dynamics. *Journal of Statistical Physics*, *107*(1/2), 143–158. <https://doi.org/10.1023/a:1014506503793>
- Roshan, H., Ehsani, S., Marjo, C. E., Andersen, M. S., & Acworth, R. L. (2015). Mechanisms of water adsorption into partially saturated fractured shales: An experimental study. *Fuel*, *159*, 628–637. <https://doi.org/10.1016/j.fuel.2015.07.015>
- Roychaudhuri, B., Tsotsis, T. T., & Jessen, K. (2013). An experimental investigation of spontaneous imbibition in gas shales. *Journal of Petroleum Science and Engineering*, *111*, 87–97. <https://doi.org/10.1016/j.petrol.2013.10.002>
- Sadjadi, Z., Jung, M., Seemann, R., & Rieger, H. (2015). Meniscus arrest during capillary rise in asymmetric microfluidic pore junctions. *Langmuir*, *31*(8), 2600–2608. <https://doi.org/10.1021/la504149r>
- Sakhae-Pour, A., & Bryant, S. L. (2014). Effect of pore structure on the producibility of tight-gas sandstones. *AAPG Bulletin*, *98*(4), 663–694. <https://doi.org/10.1306/08011312078>
- Sbraglia, M., Benzi, R., Biferale, L., Succi, S., Sugiyama, K., & Toschi, F. (2007). Generalized lattice Boltzmann method with multirange pseudopotential. *Physical Review E*, *75*(2), 95–105. <https://doi.org/10.1103/physreve.75.026702>
- Schaap, M. G., Porter, M. L., Christensen, B. S. B., & Wildenschild, D. (2007). Comparison of pressure-saturation characteristics derived from computed tomography and lattice Boltzmann simulations. *Water Resources Research*, *43*, W12S06. <https://doi.org/10.1029/2006wr005730>
- Shan, X., & Chen, H. (1993). Lattice Boltzmann model for simulating flows with multiple phases and components. *Physical Review E*, *47*(3), 1815–1819. <https://doi.org/10.1103/physreve.47.1815>
- Shan, X., & Chen, H. (1994). Simulation of nonideal gases and liquid-gas phase transitions by the lattice Boltzmann equation. *Physical Review E*, *49*(4), 2941–2948. <https://doi.org/10.1103/physreve.49.2941>
- Shanley, K. W., Cluff, R. M., & Robinson, J. W. (2004). Factors controlling prolific gas production from low-permeability sandstone reservoirs: Implications for resource assessment, prospect development, and risk analysis. *AAPG Bulletin*, *88*(8), 1083–1121. <https://doi.org/10.1306/03250403051>
- Shaoul, J. R., van Zelm, L. F., & de Pater, C. J. (2011). Damage mechanisms in unconventional-gas-well stimulation—A new look at an old problem. Paper Presented at the Journal of Petroleum Technology, Muscat, Oman.
- Singh, H. (2016). A critical review of water uptake by shales. *Journal of Natural Gas Science and Engineering*, *34*, 751–766. <https://doi.org/10.1016/j.jngse.2016.07.003>
- Son, S., Chen, L., Kang, Q., Derome, D., & Carmeliet, J. (2016). Contact angle effects on pore and corner arc menisci in polygonal capillary tubes studied with the pseudopotential multiphase lattice Boltzmann model. *Computation*, *4*(1). <https://doi.org/10.3390/computation4010012>
- Wang, Q., Guo, B., & Gao, D. (2012). Is formation damage an issue in shale gas development? Paper presented at the SPE international symposium and exhibition on formation damage control, Lafayette, Louisiana, USA.
- Warner, N. R., Jackson, R. B., Darrah, T. H., Osborn, S. G., Down, A., Zhao, K., et al. (2012). Geochemical evidence for possible natural migration of Marcellus formation brine to shallow aquifers in Pennsylvania. *Proceedings of the National Academy of Sciences of the United States of America*, *109*(30), 11,961–11,966. <https://doi.org/10.1073/pnas.1121181109>
- Washburn, E. W. (1921). The dynamics of capillary flow. *Physical Review*, *17*(3), 273–283. <https://doi.org/10.1103/physrev.17.273>
- Wenzel, R. N. (1936). Resistance of solid surfaces to wetting by water. *Industrial and Engineering Chemistry*, *28*(8), 988–994. <https://doi.org/10.1021/ie50320a024>
- Wildenschild, D., & Sheppard, A. P. (2013). X-ray imaging and analysis techniques for quantifying pore-scale structure and processes in subsurface porous medium systems. *Advances in Water Resources*, *51*(1), 217–246. <https://doi.org/10.1016/j.advwatres.2012.07.018>
- Xu, M., & Dehghanpour, H. (2014). Advances in understanding wettability of gas shales. *Energy & Fuels*, *28*(7), 4362–4375. <https://doi.org/10.1021/ef500428y>
- Yan, Q., Lemanski, C., Karpyn, Z. T., & Ayala, L. F. (2015). Experimental investigation of shale gas production impairment due to fracturing fluid migration during shut-in time. *Journal of Natural Gas Science and Engineering*, *24*, 99–105. <https://doi.org/10.1016/j.jngse.2015.03.017>
- Yang, R., Guo, X., Yi, J., Fang, Z., Hu, Q., & He, S. (2017). Spontaneous imbibition of three leading shale formations in the Middle Yangtze Platform, South China. *Energy & Fuels*, *31*(7), 6903–6916. <https://doi.org/10.1021/acs.energyfuels.7b00843>
- Ye, Y. H., Luo, C., Liu, S. G., Xiao, C., Ran, B., Sun, W., et al. (2017). Characteristics of black shale reservoirs and controlling factors of gas adsorption in the lower Cambrian Niutitang formation in the southern Yangtze Basin margin, China. *Energy & Fuels*, *31*(7), 6876–6894. <https://doi.org/10.1021/acs.energyfuels.7b00799>
- Zheng, J., Chen, Z., Xie, C., Wang, Z., Lei, Z., Ju, Y., & Wang, M. (2018). Characterization of spontaneous imbibition dynamics in irregular channels by mesoscopic modeling. *Computers & Fluids*, *168*, 21–31. <https://doi.org/10.1016/j.compfluid.2018.01.024>
- Zheng, J., Wang, Z., Gong, W., Ju, Y., & Wang, M. (2017). Characterization of nanopore morphology of shale and its effects on gas permeability. *Journal of Natural Gas Science and Engineering*, *47*(Supplement C), 83–90. <https://doi.org/10.1016/j.jngse.2017.10.004>
- Zhou, Z., Abass, H., Li, X., Bearinger, D., & Frank, W. (2016). Mechanisms of imbibition during hydraulic fracturing in shale formations. *Journal of Petroleum Science and Engineering*, *141*, 125–132. <https://doi.org/10.1016/j.petrol.2016.01.021>
- Zolfaghari, A., Dehghanpour, H., & Xu, M. (2017). Water sorption behaviour of gas shales: II. Pore size distribution. *International Journal of Coal Geology*, *179*, 187–195. <https://doi.org/10.1016/j.coal.2017.05.009>
- Zolfaghari, A., & Piri, M. (2017a). Pore-scale network modeling of three-phase flow based on thermodynamically consistent threshold capillary pressures. I. Cusp formation and collapse. *Transport in Porous Media*, *116*(3), 1093–1137. <https://doi.org/10.1007/s11242-016-0814-8>
- Zolfaghari, A., & Piri, M. (2017b). Pore-scale network modeling of three-phase flow based on thermodynamically consistent threshold capillary pressures. II. Results. *Transport in Porous Media*, *116*(3), 1139–1165. <https://doi.org/10.1007/s11242-016-0815-7>